Stick-slip and force chain evolution in a granular bed in response to a grain intruder

Antoinette Tordesillas*
Department of Mathematics and Statistics, University of Melbourne, Victoria 3010, Australia

James E. Hilton
CSIRO Mathematics, Informatics and Statistics, Clayton, Victoria 3168, Australia

Steven T. Tobin
Department of Mathematics and Statistics, University of Melbourne, Victoria 3010, Australia
(Received 9 February 2014; published 25 April 2014)

The mechanical response of granular beds under applied stresses is often characterized by repeated cycles of stick-slip. Using the discrete element method, we examine stick-slip from a concentrated force loading—imposed by a single grain that is drawn through a densely packed, periodic granular bed via a stiff virtual spring. Force chains continually form and collapse ahead of the intruder grain. A comprehensive characterization of the birth-death evolution of these load-bearing structures, along with their surrounding contact cycles, reveals a well-defined shear zone of around eight particle diameters from the intruder, encapsulating: (i) long force chains that form buttresses with the fixed bottom wall for support, (ii) a region where the collapse of the most stable, persistent three-cycles preferentially occur to the point where they are essentially depleted by the end of the first cycle of stick-slip, and (iii) an inner core where force chain buckling events concentrate. Dilatancy is greatest in this inner core, and in the region next to the free surface. During slip, secondary force chains briefly form behind the intruder: these transient force chains, most of which comprise only 3 particles, form in the direction that is roughly perpendicular to the intruder motion.

DOI: 10.1103/PhysRevE.89.042207 PACS number(s): 45.70.−n

I. INTRODUCTION

A common aspect in the mechanical behavior of many everyday materials (e.g., rubber, steel, ice, sand, wood) is the cyclic phenomenon of 'stick-slip' (e.g., [1–3]). Each cycle comprises: (i) a loading regime, or 'stick' phase, which is characterized by a rise in the macroscopic stress under small deformation; and (ii) an unloading regime, or 'slip' phase, which is characterized by a drop in stress with a corresponding large deformation. Stick-slip occurs at multiple spatial and temporal scales. Typically, the slip phase has a time scale of many orders of magnitude smaller than the stick phase [4–7]. On a large spatial scale, the most commonly recognized manifestation of stick-slip is an earthquake: the steady loading of tectonic plates may occur over a time scale of years, yet the ensuing slip event may be over in minutes [4,5]. While earthquakes span spatial scales of hundreds to many thousands of kilometers, stick-slip also manifests at the nanoscale in the motion of tips of atomic force microscopes [8]. Despite the long-standing interest in stick-slip, a detailed understanding of the process in granular materials is currently lacking. Evidence from experiments and simulations suggests this knowledge is key to our ability to control material behavior, in particular, the related processes of energy flow, shear strength and failure (e.g., [2,5,9–11]).

This study seeks to fill a knowledge gap in the current understanding of the micromechanics of stick-slip for granular materials, in particular, from the perspective of force chain evolution. The system under study involves an intruder that is dragged slowly through the bed (i.e., quasistatic motion) by a stiff spring. Before proceeding, it is instructive to briefly review past findings which are most pertinent to this study. We do not provide a comprehensive review of the literature on stick-slip nor of the granular drag literature. For a broader view of the extant literature on this topic, we refer readers to the references cited in the papers discussed here.

Various simplified models have been proposed to better understand the dynamics of stick-slip. For frictional solids, a block pulled by a spring over the frictional solid surface provides a good representation of the dynamics of stick-slip [12]. Analogous physical models have also been proposed for a granular material comprising many interacting frictional solid particles. Stick-slip behavior arising from a solid object being pulled by a spring either on the surface of or inside a granular bed has been explored. Nasuno *et al.* [6] investigated a planar Couette setup, where a heavy frictional plate was pulled over a particle bed by a stiff spring. The plate was found to exhibit stick-slip behavior at low speeds [6]. Albert *et al.* [7] provide a particularly detailed study of a stick-slip behavior arising from a rod attached to a stiff spring that is drawn through a rotating particle bed. Metayer *et al.* [13] observed stick-slip behavior in rods pulled vertically from granular packings. In all of these studies, the macroscopic stick-slip behavior is induced by a load that is applied via a spring. In the present study, the spring is 'virtual': i.e., it only interacts with the intruder and not with other particles in the bed. Hence, we can examine the effects of the intruder on the bed in isolation from any effect of a spring.

The link between the dynamics and underlying microstructural mechanisms of stick-slip has also been investigated for various granular materials under compression and shear (e.g., [2,7,10,14–16]). These studies suggest a connection between stick-slip and the dual nature of force transmission

*atordesi@ms.unimelb.edu.au

in granular systems [17]. In particular, stick-slip dynamics appears to be driven by the collective evolution of force chains, i.e., self-organized columnar structures comprising particles which carry the majority of the load in the system (e.g., [18,19]). These structures, belonging to the so-called strong network, continually align in the direction of the compressive principal stress, and are thus axially loaded. Surrounding the force chains are the particles in the complementary weak network that provide necessary lateral support to the force chains. Using photoelastic disk assemblies, experiments directly revealed the tie between the creation and collapse of force chains, and the rises and falls in the macroscopic shear stress [3,10,14,20–22].

Observations of these stress fluctuations strongly suggest that the stick phase is governed by the formation of force chains, while the slip phase is due to the collective failure of force chains by buckling and elastic unloading. During the stick phase, stored elastic strain energy builds up at the contacts between the constituent particles of the force chain. This build up of stored energy during stick cannot, however, continue indefinitely. Force chains are highly unstable structures and, like architectural columns, are prone to fail by buckling when overloaded to some critical value. Thus, once a critical threshold is reached, the slip phase initiates: force chains buckle and all the stored energy accumulated at their constituent contacts is collectively released. Studies of granular drag [1,7,23,24] and granular shearing [2,16] have also shed considerable light on the possible role of force chains and, in particular, the influences of particle surface and shape (e.g., brass, wood, pasta) on force chain stability and, in turn, on the dynamical features of the observed fluctuation (i.e., random versus periodic). Studies of data from experiments on photoelastic disk assemblies [21,25,26], supplemented by discrete element simulations [18,19,27–29] further characterize the topology and dynamics of force networks and their relationship to stick-slip.

This study is part of a broader, two-pronged effort to examine stick-slip dynamics and micromechanics across multiple scales in space and time. The first prong is devoted to the mesoscopic scale, the objective of which is to characterize the evolution of force chains in photoelastic disk experiments and simulations under quasistatic loading conditions. The second prong focuses on the macroscopic scale, and is focused on the characterisation of the underlying dynamics from time series measurements of stress. This study belongs to the first prong. An earlier investigation in the first prong examined the evolution of cluster configurations [25] in photoelastic disk assemblies under cyclic biaxial shear. There force chains were found to inhabit favored cluster conformations in distinct stability states, which implies preferred structures during stick events and their ensuing collapse during slip events. Accompanying that study was an investigation in the second prong that explored the dynamics of stick-slip for a series of slider experiments [30]. Each experiment comprised a bed of photoelastic disks that is sheared by a rough slider pulled along the surface by a stiff spring. Individual stick-slip cycles were found to exhibit dynamics richer than a linear description, in particular, one involving a nonlinear determinism. The active degrees of freedom detected from the data within each cycle suggests that a real physical evolution law describing stick-slip must contain at least four to six state variables. From a continuum mechanics standpoint, this finding supports nonlocal continuum theories which can account for the effects of grain rotations (e.g., Cosserat or micropolar formulations), which are a crucial element of force chain buckling [22]. The bed was also found to have no long-term memory across cycles, which makes physical sense since stick-slip events temporally far apart in the experiment are due to force chain structures in different parts of the granular bed. The system studied here is similar to the experiment in [30], to the extent that the intruder only travels on undisturbed parts of the bed.

Despite the above advances, no attempt has yet been made to establish whether such well-defined behavior arises only when the external load is applied over a relatively large area encompassing many grains. To shed light into this problem, this study is devoted to unravelling the nature of stick-slip arising from a concentrated loading condition imposed at the scale of a single grain [31]. To achieve this, we take advantage of computational modeling to simulate the motion of a single grain intruder, a test that would be very difficult to realize experimentally. Our aim is to individually track, and take precise measurements of, the dynamics and microstructural rearrangements occurring within the system. Like the slider experiments examined in [30], we also focus on stick-slip arising from a solid intruder that is pulled along at a constant velocity via a spring. However, unlike the slider, the intruder is a single grain having the same representative size and shape as the particles in the bed and, moreover, is fully immersed and dragged inside the bed by a virtual spring (i.e., the spring itself does not interact with or disturb the bed). The forces imposed on the bed by the intruder grain provide the smallest possible perturbation to a granular system. This setup therefore allows the response of the system from the smallest allowable perturbation to be carefully tracked and measured. All of the previous experimental studies on stick-slip have involved measurements of granular behavior in response to bulk forces applied over many grains (i.e., large sections of the bed). In such cases, it is difficult to separate the effects of loading and the subsequent response of the granular bed on an individual particle basis. Of specific interest in this study is to uncover the difference, if any, in the details of force chain and contact cycle evolution from a grain intruder versus a solid object that is large compared to the grains in the bed. The rest of this paper is arranged as follows. The discrete element model is described in Sec. II. We next describe our strategy in Sec. III, before presenting our results in Sec. IV. We conclude with a summary of key findings and a direction for future research in Sec. V.

II. DISCRETE ELEMENT MODEL

In this study the Discrete Element Method was used as the computational model for simulating the system (Fig. 1). Particle positions and velocities were individually resolved using time integration of the equation of motion for every particle in the system:

$$m_i \frac{\mathrm{d}\mathbf{v}_i}{\mathrm{d}t} = \mathbf{F}_n + \mathbf{F}_t + m_i \mathbf{g}, \tag{1}$$

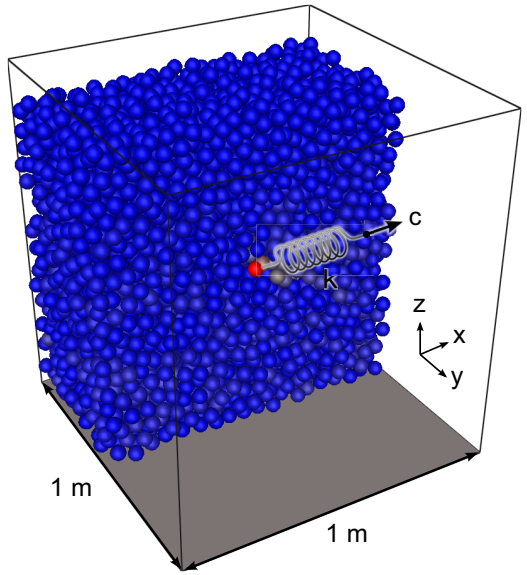

FIG. 1. (Color online) Setup of system, shown in cross section, comprising a static granular bed in a 1 m^3 periodic domain with a central particle (the intruder-grain) attached to a spring with stiffness k. The free end of the spring moves at a velocity c.

where m_i is the mass of particle i and $\mathbf{v}_i$ is the particle velocity. The forces in this equation of motion were modeled using a 'soft-sphere' approach in which contacting particles have a small overlap of length $\delta\mathbf{l}$. Here, this overlap was restricted to around $\sim$0.001% of the particle diameter. The particles were subject to a linear spring-dashpot force in the normal direction, F_n, given by

$$\mathbf{F}_n = -k_n\delta\mathbf{l} + C_n\mathbf{v}_n, \tag{2}$$

where C_n is a normal damping coefficient, k_n is a spring stiffness, and $\mathbf{v}_n$ is the relative normal velocity between the particles. In this implementation, the spring stiffness and coefficient of restitution were fixed and the normal damping coefficient was calculated to give the required normal coefficient of restitution [32]. In the contact plane, particles were subject to a second linear spring-dashpot force, F_t, limited by Coulomb friction:

$$\mathbf{F}_t = \min\left[\mu\mathbf{F}_n, k_t\int \mathbf{v}_t\,dt + C_t\mathbf{v}_t\right], \tag{3}$$

where $\mathbf{v}_t$ is the relative tangential surface velocity, μ is the coefficient of friction between the particles and the walls, C_t is a tangential damping coefficient, and k_t is a tangential spring stiffness which was chosen to be $k_t = k_n/2$. The integral term models a tangential elastic deformation of the surface, which is limited by Coulomb friction $\mu\mathbf{F}_n$. Further details of the model and validation cases are given in Refs. [33,34].

A computational domain of 1 m^3 was used, with a solid base in the negative y direction and a free surface in the positive y direction. Periodic boundary conditions were applied in the x and z directions. Ideally, the simulations would be carried out in a very large bed to ensure any boundary effects were negligible. Unfortunately, this was computationally intractable with the very stiff particles used in our study. Periodic boundaries were used as they had the advantage of providing a time-independent boundary effect, in contrast to solid boundaries. In this setup, solid boundaries would have had a strongly time dependent effect as the intruder approached the boundary. Any boundary effects resulting from periodicity in this case were only due to forces bridging between periodic copies of the intruder. Through the investigations carried out for this study, we believe any such bridging effects were negligible in comparison to the force from the virtual spring. The particle density was 1000 kg/m^3, with a coefficient of restitution of 0.5. The domain was initially filled by creating spherical particles at the top of the domain and allowing them to freely fall under gravity. Particles were given a slight polydispersity to prevent crystallisation effects, with diameters ranging from 5.1 cm to 4.9 cm. A total of 9498 particles were used in the simulation. A comparatively large value for the linear spring constant was used, $k_n = 10^7$ N/m, giving a time step of $\Delta t = O(10^{-6})$ s, to ensure highly accurate simulations.

Loading was imposed on the system by attaching the particle initially closest to the center of the domain to a virtual spring. This particle, regarded as the intruder, was not constrained in any way, apart from the additional force added by the spring. The spring was stretched by moving the free end at a constant speed of $c = 0.01$ m/s along the x-axis. The spring constant used for the virtual spring was $k = 1000$. This setup is shown schematically in Fig. 1, where the central intruder particle is colored red (color online).

Finally, we note that we have carried out a number of simulations for different domain dimensions to ensure the application of periodic boundary conditions did not affect the stick-slip characteristics. For example, for a domain that is twice the width and depth of the system considered here, we found comparable spring force characteristics within similar minimum and maximum bounds. Moreover, we also found the volume fraction of the bed to remain almost constant over the duration of the simulation. The largest change was around the first slip event, with a drop in volume fraction of approximately 0.2%. Therefore, we do not consider the microstructural trends uncovered here to be dependent on any settling effects within the bed.

III. STRATEGY FOR CHARACTERISATION

The stick-slip response of the granular bed to the moving intruder is shown in Fig. 2. This is composed of linear loading cycles in the spring force, with sudden sharp drops giving the characteristic sawtooth pattern of stick-slip behavior. The intruder velocity shows sharp spikes corresponding to the sudden movement of the intruder during each slip event. The question we seek to answer concerns the mechanisms underlying: (i) stick, (ii) slip, (iii) dilatancy, and (iv) emergent zones of deformation around the intruder. Although these aspects of mechanical response are intertwined, (i) and (ii) deal directly with force transmission, while (iii) and (iv) can be quantified through the contact topology and grain kinematics. During stick, the particles in the bed continually adjust their contacts and contact forces to resist the increasing force from the intruder, although the overall deformation of the bed remains small. During slip, large grain rearrangements occur allowing the intruder to advance forward. We will characterize the mechanisms underlying stick and slip by tracking the birth

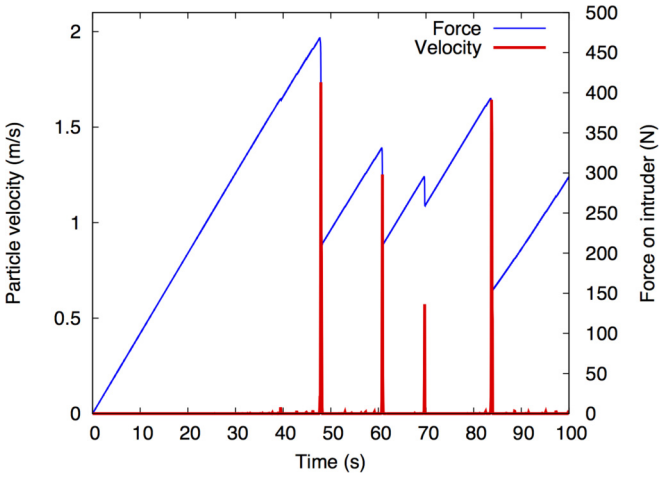

FIG. 2. (Color online) Spring force and intruder velocity for a system with $\mu = 0.3$. Sharp peaks in the velocity of the intruder coincide with drops in the spring force, which correspond to slip events.

and death evolution of structural building blocks of m-force chains and n-cycles, as illustrated in Fig. 3. The methods we employ for identifying m-force chains and n-cycles, and their evolution, are explained in detail elsewhere (e.g., [19,26]). Only a brief summary is given here for completeness.

For each time state in the simulation, we construct a complex network (or mathematical graph) to represent the connectivity of the grains in the bed. Each particle is represented by a vertex in this contact network, and two vertices are connected with an edge if the corresponding physical particles

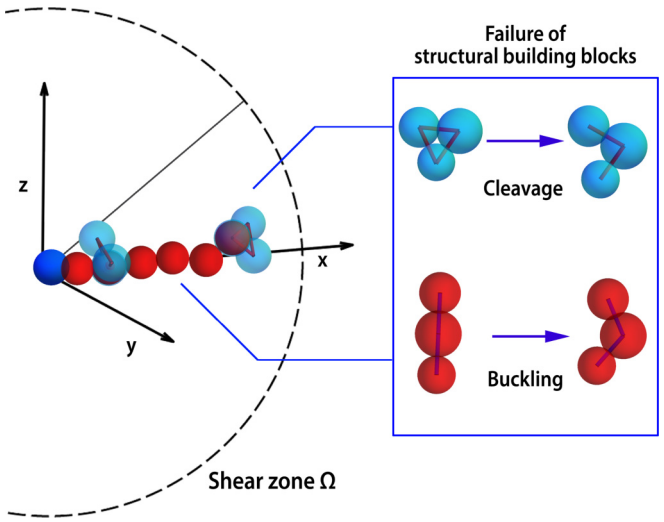

FIG. 3. (Color online) From simulation, force chains (red spheres) are formed ahead the intruder (dark blue sphere), moving in the direction of increasing x (left). The force chain is supported by contacts in varying local topologies. Shown are those in a 'three-cycle' formation with the force chain: three particles in mutual contact (light blue spheres). Larger size contact cycles, although present, are not shown for clarity. Illustration of key failure events occurring in the shear zone include: three-cycles breaking apart by cleavage and force chains buckling (right).

are in contact. The resulting contact network is unweighted and undirected. This abstraction focuses only on the *connectivity* of the physical system, as defined by the contacts between particles. The granular bed's response recorded at the current time state τ may represent a combination of information taken from the previous time state $\tau - d\tau$ and the current time state τ. For example, the birth (death) of a structural building block is marked by its absence (presence) at $\tau - d\tau$ followed by its appearance (collapse) at τ.

The *linear building blocks are the m-force chains*, where $m \geqslant 3$ is an integer denoting the number of particles that form this physical structure. These are identified using a quantitative method previously employed by Tordesillas and co-workers (e.g., [18,35,36]). This method requires information on the contact forces and their orientation, in addition to the contact network. Particles in force chains can be identified using their particle load vectors (PLVs), which are derived from the local force moment tensor s_{ij} of each particle:

$$s_{ij} = \sum_{c=1}^{\alpha} f_i^c r_j^c, \tag{4}$$

where α is the number of contacting neighbors of the particle, and f_i^c and r_j^c denote the components of the contact force and the unit normal vector from the center of the particle to the point of contact. The magnitude of the PLV is given by the largest eigenvalue of s_{ij},

$$\frac{s_{11} + s_{22}}{2} + \sqrt{\left(\frac{s_{11} - s_{22}}{2}\right)^2 + s_{12}s_{21}}; \tag{5}$$

the direction of the PLV is given by the corresponding eigenvector. A force chain is defined as a chain of three or more particles in contact, whose PLV magnitudes all exceed a global average value and all align. That is, for each particle in the force chain the angle between the PLV and the branch vector (i.e., the vector connecting the reference particle center to the center of its contacting neighbor in the force chain) must be less than the tolerance angle, here chosen to be 45°. The global average value of the PLV magnitude varies with time in a qualitatively similar manner to that of the shear stress. In particular, it reaches a peak value at the same time as the peak shear stress.

To identify m-force chains that buckle during a given time interval $[\tau - d\tau, \tau]$, we find those force chains whose axial load decreases as constituent members misalign and displace laterally relative to their initial configuration at $\tau - d\tau$. This is achieved through a three-step process of elimination.

(1) Eliminate all particles that are not in force chains at the initial time $\tau - d\tau$, leaving only force chains.

(2) From the force chains remaining after step 1, eliminate those whose constituent particles do not individually experience a drop in PLV magnitude during $[\tau - d\tau, \tau]$.

(3) From the force chains remaining after step 2, eliminate those that do not contain at least one contiguous three-particle segment that misaligns by at least a prescribed threshold buckling angle, θ^*, during $[\tau - d\tau, \tau]$.

Although the system in this study is three-dimensional, an illustration in 2D of the third and final step above is useful to aid visualisation. Consider the example in Fig. 4. Suppose the

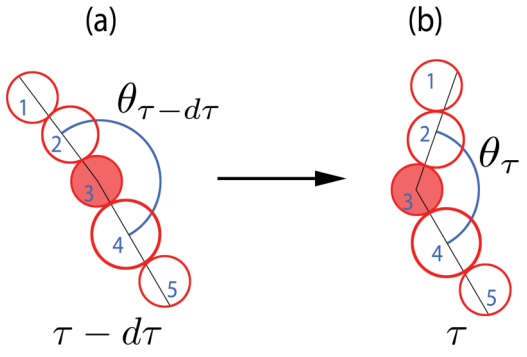

FIG. 4. (Color online) A force chain buckles during $[\tau - d\tau, \tau]$ if $\theta^* < (\theta_{\tau-d\tau} - \theta_\tau)/2$ (the third stage in our buckling force chain identification process). In this example, the five-force chain buckles at particle 3 in the segment 2-3-4.

five-force chain shown is one of the force chains to be analysed in step 3. A five-force chain has three contiguous segments (1-2-3, 2-3-4, and 3-4-5). We represent the change in alignment of each such force chain segment via the buckling angle θ, given by $\theta = (\theta_{\tau-d\tau} - \theta_\tau)/2$, where $\theta_{\tau-d\tau}$ and θ_τ are the subtended angles of the two outer particles in the segment with respect to the central particle at the times $\tau - d\tau$ and τ, respectively, and $0 < \theta_\tau < \theta_{\tau-d\tau} \leqslant \pi$. We deem that a force chain segment (and hence the force chain of which it is part) has buckled when the buckling angle exceeds a prescribed threshold θ^*, i.e., $\theta^* < \theta$. The sensitivity of the procedures described above to the chosen thresholds values has been studied extensively using both experiments and simulations [18,22,35–37]. Such studies suggest that our threshold choices are physically reasonable and produce consistent trends for different loading conditions and material properties.

The *cyclic building blocks are the n-cycles*, where $n \geqslant 3$ is an integer denoting the number of edges or particles that form the structure in the abstract domain of the complex network or physical domain, respectively. For example, a three-cycle in the complex contact network corresponds to three particles in mutual contact in the physical sample. The n-cycles are identified from the minimal cycle basis of the contact network (e.g., [19,26]). This basis is a set containing the shortest cycles, or the cycles with the minimum length or number of edges of the contact network. An n-cycle is thus a non-intersecting walk (or closed path) of length n where $n \geqslant 3$, containing no repeated vertices (other than its initial and final vertex) [38]. There are a number of established algorithms for obtaining a minimal cycle basis for a complex network. We use the algorithm of Horton [39] in conjunction with a faster variant presented by Mehlhorn and Michail [40]. The collapse or death of an n-cycle during $[\tau - d\tau, \tau]$ occurs by cleavage and is simply marked by its presence at $\tau - d\tau$, followed by the collapse of one or more of its edges or contacts at τ.

IV. RESULTS

In what follows, we first focus on the *temporal evolution* of structural building blocks with respect to the interrelated aspects of the stick phase, during which the greatest resistance to intruder motion is mobilized in the bed; the slip phase, during which the bed's resistance drops allowing intruder to move; and dilatancy. Next, the *spatial distributions* of the building blocks are explored, in particular, how the different size building blocks are organized around the intruder. Here attention is paid to the existence of emergent zones, most importantly the shear zone. Finally, we tie these spatial trends to the earlier results on temporal evolution to understand how the material's structure evolves. Which building blocks does the bed create more (or less) of as the intruder moves through the bed? What is the load allocation among the force chains and how does this relate to their spatial distribution in the bed? How are the different building blocks adapted and reorganized to resist the intruder's motion through the bed? How do any of these trends differ from those seen for large solids interacting with a granular bed (e.g., a punch penetrating a bed), given that the intruder is of comparable size to the particles in the bed?

A. Temporal evolution of structural building blocks

The mechanical response of the bed to the moving intruder, shown in Fig. 2, comprises interlacing periods of increasing resistance (stick) and failure (slip), as evident in the rises and relatively brief falls in the spring force exerted by the material on the intruder.

In Figs. 5 and 6, we show the spring force along with the population of structural building blocks from self-organization of the bed. Large fluctuations manifest in the populations of

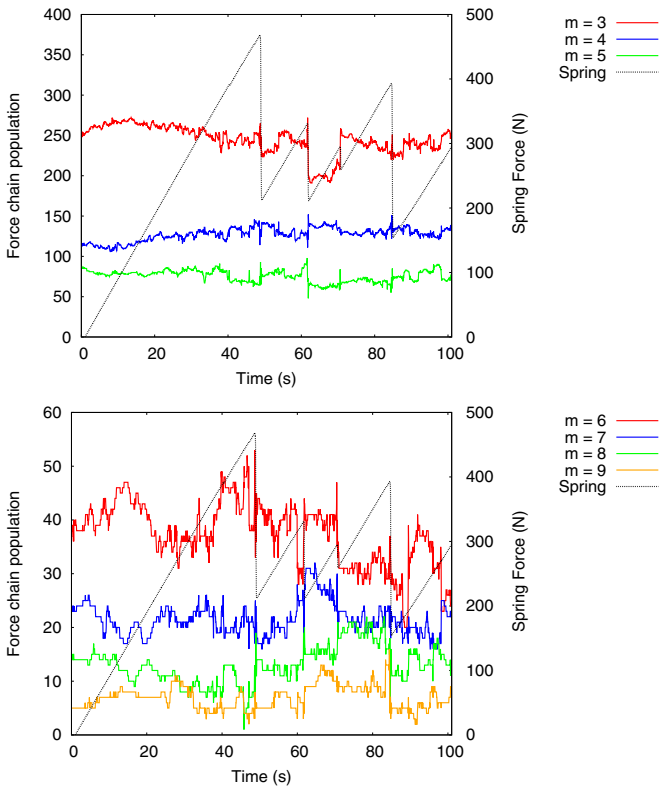

FIG. 5. (Color online) Evolution of the population of linear structural building blocks, m-force chains, where m is the number of particles in the chain. Short force chains (m = 3,4,5 [top]) are more common than long force chains (m = 6,7,8,9 [bottom]). The spring force F is also plotted.

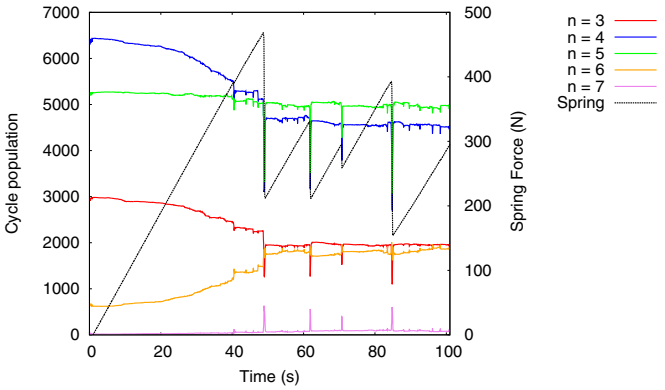

FIG. 6. (Color online) Evolution of the population of cyclic structural building blocks, n-cycles, where n is the number of particles in the cycle. Small cycles (n = 3,4,5) and large cycles are shown (n = 6,7). Dilation of the bed in the stages leading up to the first slip event can be seen in the decrease in small three-, four-, five-cycles amidst an increase in six-, seven-cycles.

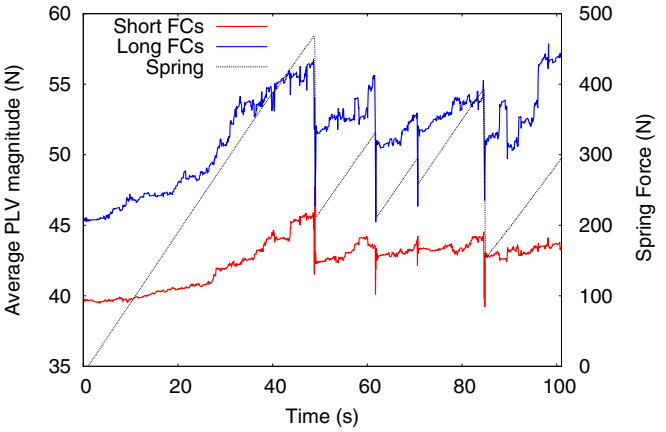

FIG. 7. (Color online) Load carrying capacity of force chains. Temporal evolution of the average particle load vector magnitude of short and long m-force chains for low resolution. Long force chains carry more load than the shorter force chains.

m-force chains; however, no distinct, long-term pattern of variation (decrease/increase) with respect to the entire loading history is evident, nor is there a consistent trend during slip or stick events. The relative populations of m-force chains are in accord with all past observations of dense samples under varying loading conditions and material properties: that is, three-force chains dominate, with the population of each class decreasing as m increases (e.g., [19,26,41–43]). By contrast, the relative populations of the minimal contact n-cycles do not exhibit a consistent pattern of dominance with respect to n. The smallest members (i.e., three-cycles) do not dominate the bed, with the population decreasing with increasing n as seen, for example, in localized failure samples (e.g., [19,26,42,43]). Instead the four-cycles are the most populous, followed by the five-cycles and then the three-cycles. Nonetheless the temporal evolution of the population of three-cycles is qualitatively similar to that of the four-cycles. Both undergo a steady decline in population prior to the first slip event, followed by a near invariant temporal evolution except during slip events when the population undergoes a sharp drop. The five-cycles maintain an almost constant population throughout loading except during slip events when they undergo a sharp decline in numbers, like the three-, four-cycles. In past studies [41], we found that the dominance of four-, five-cycles in the bed does not in any way weaken the functional role that three-cycles play in reinforcing force chains. There, the degradation of three-cycles also proved to be an excellent bellwether for collective failure by buckling of force chains.

By far the greatest difference between the process of self-organization in this system versus those seen from systems where large portions of the granular material are influenced by the applied loading [26,41–44]—lies in the sharp changes in n-cycle population during slip. In [26,41–43], the temporal evolution of n-cycles does not closely track any features of the macroscopic stress or applied force. Here we observe a strong correlation between slip events and the sudden drop (rise) in population of the smallest three-, four-, five-cycles (six-, seven-cycles).

1. The stick phase

The increasing resistance from the bed during the stick phases, as evident in the rise in the spring force, is mostly borne by the principal load bearing structures of force chains [36]. This increasing resistance to the intruder occurs while there is progressive loss of lateral support, as evident in the decreasing population of small three-, four-cycles in the bed (Fig. 6). On average, the long force chains provide the greatest resistance to the moving intruder (Fig. 7). A similar trend was observed in the shallow penetration of a granular bed by a rectangular punch [43]. However, this load allocation is far from obvious. As found in 2D experiments and simulations [26], longer force chains are less stable than shorter force chains; hence, one might expect the former to carry less load than the latter. Cooperative evolution between force chains and three-cycles (previously established for other 2D and 3D systems, e.g., [19,41,42]) is shown in Fig. 8 with an equal partition of support to short and long force chains observed. Relative to particles in non-force chains, however, a distinct pattern is evident: particles in force chains not only have a higher number of supporting contacts but more of their contacts are in three-cycles. These aforementioned trends on cooperative behavior between force chains and three-cycles apply also to the most dominant class of cyclic building blocks: that is, the four-cycles also support the force chains in a qualitatively similar manner as the three-cycles (data not shown).

2. The slip phase

We have already seen the progressive loss of three-, four-cycles during the initial stages of loading in the first stick phase. The degeneration of these small cycles has ramifications for the stability of the loading-bearing force chains and, in turn, the granular bed. As previously mentioned, force chains, like architectural columns, fail by buckling [18,26]. The degradation of the lateral supporting structures of three-, four-cycles, render force chains particularly prone to collapse by buckling: Fig. 9.

To gain a detailed understanding of processes occurring in the bed, we now "zoom-in" on the three major slip events.

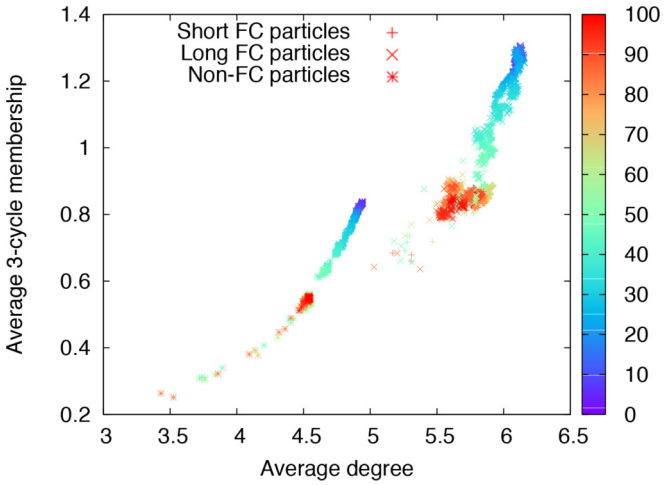

FIG. 8. (Color online) Cooperative evolution of columnar force chains and truss-like three-cycles. Average three-cycle membership versus average degree for particles that make up long and short force chains, and non-force chain particles. A distinct split is visible between those particles that belong to force chains and those that do not, but no clear difference is apparent between short and long force chains.

Figure 10 shows the temporal evolution of the load borne by the long and short force chains, here measured by the average magnitude of their particle load vectors [recall Eq. (5)]. Four aspects of behavior can be gleaned from these distributions. The first relates to the fluctuations, which suggest that there are significant grain rearrangements and force reconfigurations occurring during all three slip events. The second concerns the multimodal character of these distributions; this is similarly evident in the population of buckling force chains (Fig. 11). This may be caused by multiple slip events ('micro-slips') occurring in close succession of each other. The third is the underpinning mechanism for failure and slip, which is most evident in Fig. 11. Observe here that the sharp bursts in the population of mesoscopic failure events, i.e., the failure of

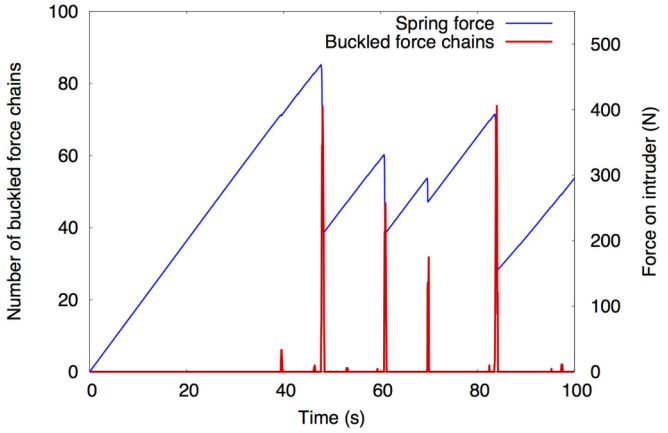

FIG. 9. (Color online) Spring force F and failure by buckling of force chains as a function of time. Only force chains that have buckled by an angle of at least $\theta = 1^\circ$ are counted. It is readily apparent that buckling events spike sharply during the slip phases, while the spring force is rapidly decreasing.

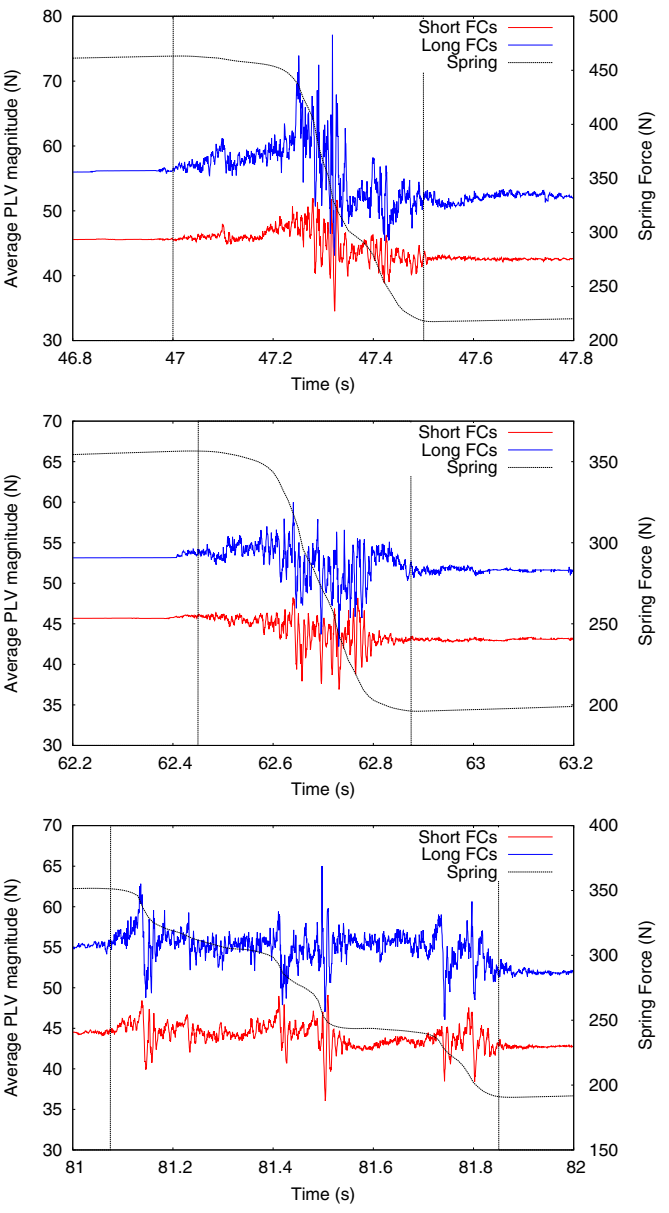

FIG. 10. (Color online) Load carrying capacity of force chains. Temporal evolution of average particle load vector magnitude of short and long m-force chains for three high-resolution slip events. Long force chains carry more load than the shorter force chains. A complex multi-stage failure process is evident in all three slip events (demarcated by vertical dashed lines).

the structural building blocks of force chains by buckling and the cleaving of three-cycles, precipitates an overall loss of resistance of the bed to the moving intruder. In comparing the first stick event in Fig. 6 and the first slip event in Fig. 11, a lag between two key failure events can be observed: the steady loss of supporting three-, four-cycles in the bed during the first stick event, followed by the failure of force chains by buckling, and the further but more dramatic loss of three-cycles in the first slip event. Force chain buckling is an inherently dilatant rearrangement event: three-, four-cycles conjoined with the chain open up and become bigger cycles as the force chain misaligns and separates from its immediate

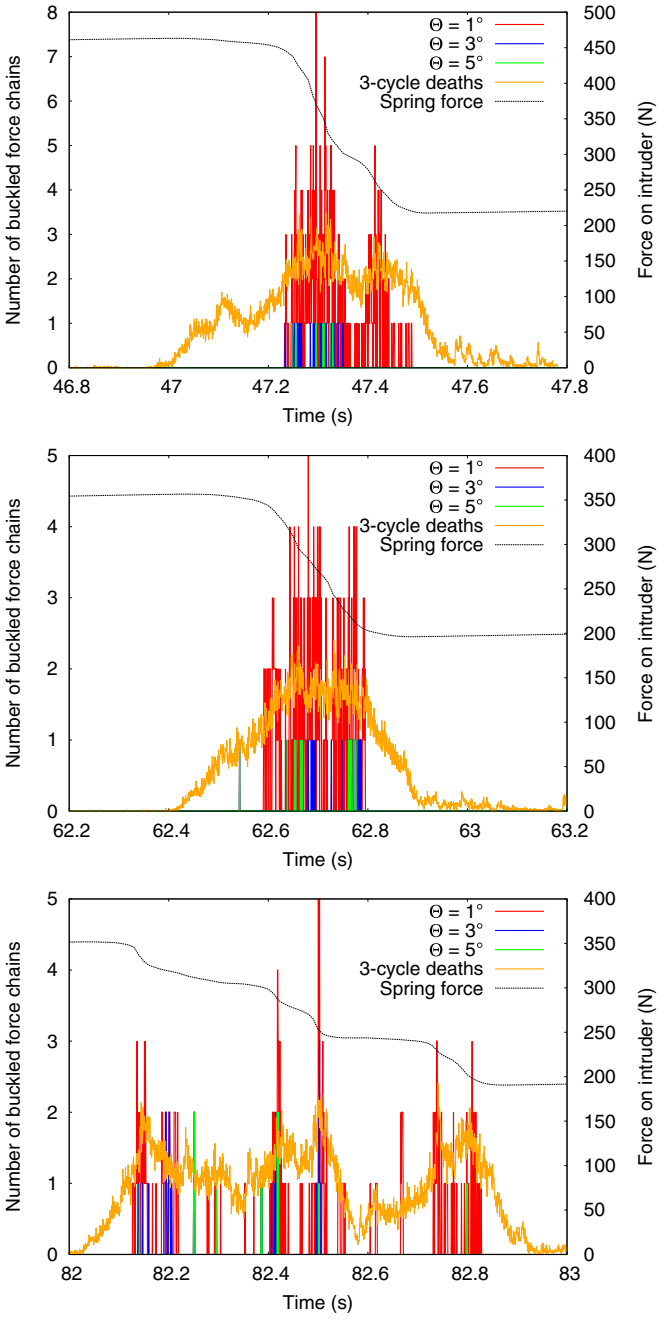

FIG. 11. (Color online) Spring force F and failure of structural building blocks for high resolution slip (the same events shown in Fig. 10). Population of force chains that have buckled by at least an angle θ, and three-cycles that cleaved, with spring force on the intruder. The populations of failure events are computed over a uniform sequence of time increments (in this case 5 simulation timesteps or 0.003 s) and plotted at the end of the increment.

neighbors during buckling. Moreover, the energy released from buckling drives dilatant rearrangements among weak neighbors. These processes are evident in Fig. 12, which show that the collapse of small three-, four-, five-cycles gives way to larger six-, seven-cycles. The fourth concerns the distinct peaks in the average PLV magnitude during slip events in Fig. 10, suggesting sudden increases in load for some force chains

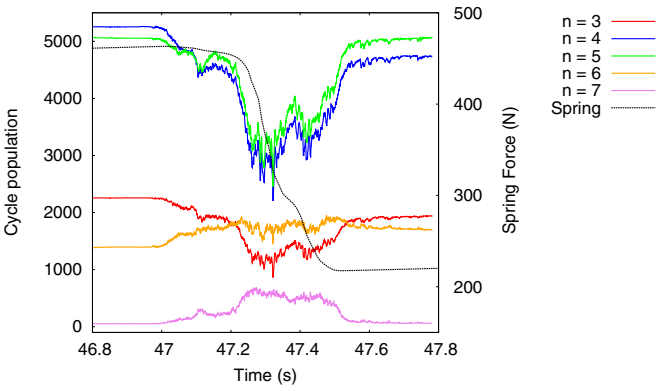

FIG. 12. (Color online) The relative populations of n-cycles show the development of dilatancy in the granular bed. As the small cycles (i.e., three-, four-, five-cycles) break apart, a corresponding increase in the population of six-, seven-cycles is observed. This suggests that the cleaved short cycles are joining together to form larger cycles, dilating the bed.

and/or that new force chains form while collective force chain buckling is active in the bed. These somewhat contradictory processes merit further study and we will attempt to unravel this pattern later in the next section.

B. Spatial evolution of structural building blocks

Here we examine the spatial evolution of the structural building blocks that form in the bed. Attention is paid to the zone of influence, i.e., the shear zone Ω, and the different partitions therein (recall Fig. 3). Our working hypothesis is that the structural building blocks behave in distinct ways depending on their location in the bed, and that this can be viewed as a manifestation of their changing functionalities with respect to load transfer in the different sectors of the bed. In what follows, we will elucidate these patterns along with the ways that the building blocks adapt and reorganize to resist the intruder motion as it moves through the bed. We proceed in two steps. First, we will identify the location and shape of the shear zone Ω. Second, we will identify in this zone where the following structures and processes and develop: (i) force chains and three-cycles, (ii) failure of three-cycles and force chains, (iii) dilatancy, (iv) a "wake" region behind the intruder, and (v) an undeforming cluster of grains (the so-called "dead-zone") that forms in front of, and moves with, the intruder in rigid body motion [44]. From here onwards, we will solely focus on the first slip event as trends uncovered here also apply to subsequent slip events.

1. Shear zone

By far the most revealing of the boundary of Ω are the spatial distributions of failure events. The spatial distribution of buckling force chains is shown in Fig. 13. Buckling mainly occurs in front of and below the intruder, as the grains in the bed rearrange to oppose the motion of the intruder. Figure 14 shows the location of the buckled segments of the force chains during the first slip event; this shows where the greatest misalignment occurred, rather than the entire chain. This reveals a zone that is circumscribed by a sphere with radius $r = 4d_m$ centered on

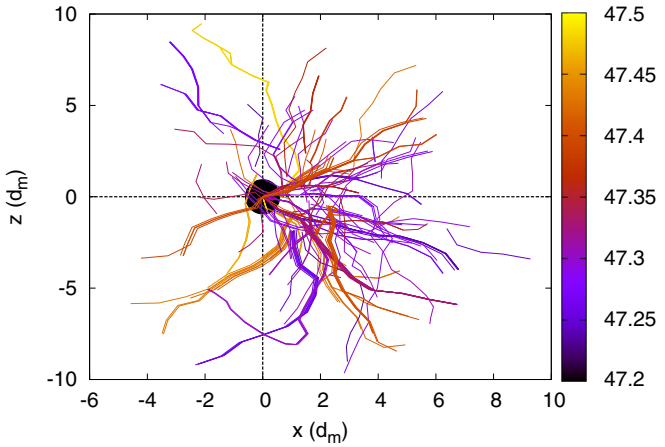

FIG. 13. (Color online) A spatial plot of all force chains that buckle, accumulated during the first slip event and colored by time (all force chains are plotted with equal line thickness). Positions of buckling force chains are identified relative to intruder center at the origin (0,0). While a large majority of buckling force chains are ahead of the intruder (resisting its motion through the bed), we note the existence of force chains behind (aft of) the intruder.

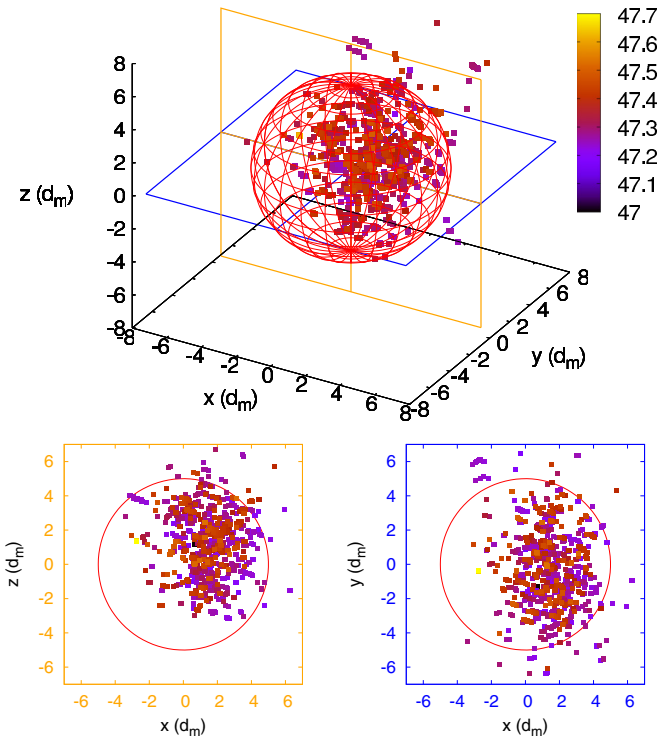

FIG. 14. (Color online) Shear zone from the perspective of buckling force chains. By plotting the centroids of the buckling force chains (specifically the three-particle segments of the chain where the buckling occurs), a clear zone of influence becomes apparent. This zone is within a radius of $r = 4d_m$ from the origin where the center of the intruder is located. The large majority of such buckling events occur within this zone of influence (top). The 2D projections of this data (bottom row) lends further clarity to the boundary of this sphere of influence.

the intruder, where d_m is the mean particle diameter. Based on past studies of force chain buckling around intruders [35,43], this zone is most likely a subset of Ω; that is, we expect the zone of influence to be beyond this inner core. This is confirmed in the spatial distributions of force chains in Fig. 15. The short ($m = 3,4,5$) force chains tend to be more evenly spread in the bed when compared to the long ($m > 6$) force chains (Fig. 15). The long force chains tend to be clustered ahead of the intruder, extending well into the fixed wall at the bottom. A plausible explanation for this is that force chains resisting the intruder can brace against this wall and use it as leverage against buckling. This 'buttressing' behavior has been previously observed in cone penetration tests [45]. An example of a force chain acting in this manner can be seen in Fig. 16.

We may extend our analysis of the shear zone Ω by remembering that three-cycles in the granular bed support and protect the load-carrying force chains. Therefore, force chain buckling will normally be preceded and accompanied by loss of three-cycles by cleavage, and we may use the spatial distribution of these structures to check our candidate Ω. Figure 17 shows the radial distribution of particle three-cycle membership (i.e., how many three-cycles on average a particle some distance r from the intruder will have). We note an inflection point at $r \approx 4d_m$, suggesting that the zone identified from the spatial pattern of force chain buckling is indeed part of the shear zone.

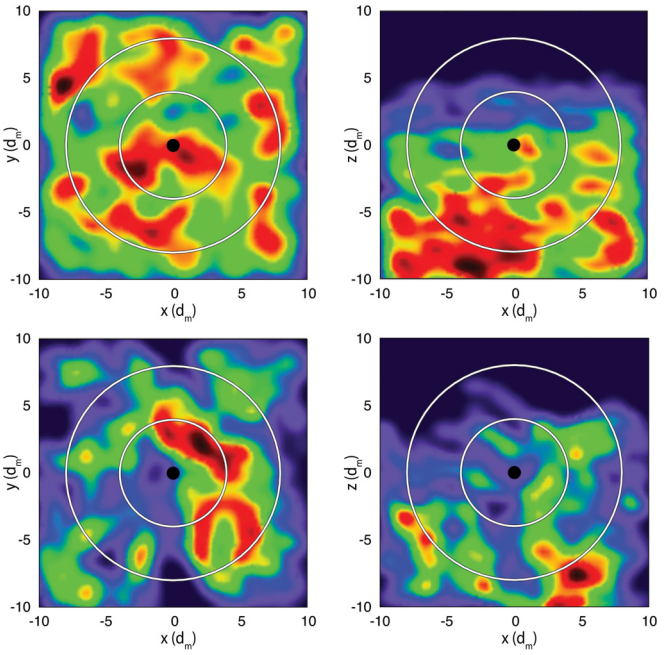

FIG. 15. (Color online) Representative spatial distributions of major load-bearing structures at the end of the first stick event projected on to 2D planes, with the left column images projected to a horizontal plane ($z = 0$) and the right column images projected to a vertical plane ($y = 0$). The short force chains ($m = 3,4,5$) are shown in the top row, and long force chains ($m = 6,7,8,9$) are shown in the bottom row. The short chains are more evenly spread through the bed, while the long chains exhibit a preference for the region of the bed ahead of the intruder, with another bias towards the bottom of the bed. The concentric circles mark $r = 4d_m$ and $r = 8d_m$, the candidates for the shear zone.

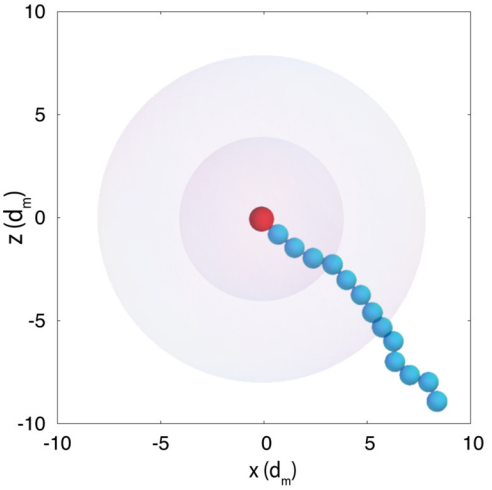

FIG. 16. (Color online) Plotting the force chains born during a single timestep (in the first stick phase) provides a clear example of a 'buttress' force chain, extending down from and ahead of the intruder (center). Such chains brace themselves against the fixed bottom wall of the bed (not shown), allowing a greater resistance to the intruder's motion.

2. *Spatial distribution of n-cycles*

The full shear zone can be probed by considering the spatial distribution of a special subset of the three-cycle population, the so-called "persistent three-cycles". Persistent three-cycles are those which have survived from the beginning of loading to the stage in question and, as such, are the most stable three-cycle structures in the system [42,46]. In previous studies of biaxial and triaxial compression tests, the destruction of this sub-group of three-cycles was confined to within that region where the shear band ultimately develops [42,46].

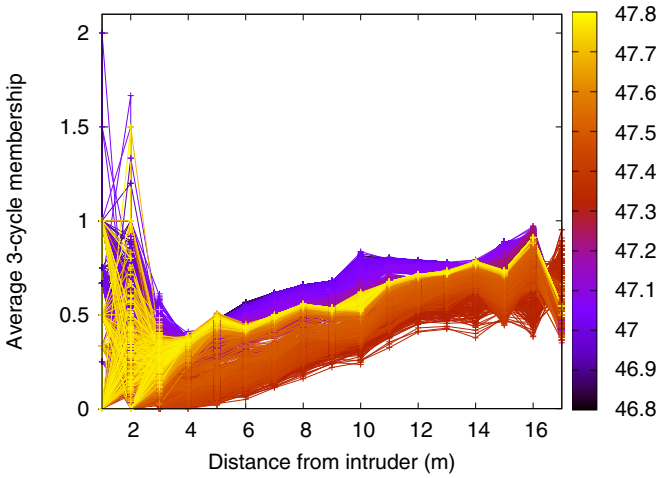

FIG. 17. (Color online) Ω from the perspective of three-cycle population. The graphs show the average three-cycle membership of the particles a distance r from the intruder, with color indicating time during the first slip event. The presence of an inflection point at $r \approx 4d_m$ indicates the existence of a shear zone within that volume. Note also that as the slip event progresses the average three-cycle membership throughout the bed first falls, then recovers.

Furthermore, these persistent structures become essentially depleted in the shear band once the band is fully developed. Here we observe a similar trend occurring in a region that is twice that identified earlier from the location of buckling force chains. We observe progressive degeneration of persistent three-cycles to be confined to a shear zone of around eight particle diameters from the center of the intruder, with the population inside reaching negligible values by the end of the first cycle of stick-slip (Fig. 18). The spatial pattern of dilatancy from death (birth) of small three-, four-, five-cycles (large six-, seven-cycles) corroborate this result; recall the temporal pattern was presented earlier in Fig. 12. We observe from Fig. 19 that most of the three-, four-, five-cycles cleave within $r = 8d_m$ from the intruder; keep in mind that the top of our system is a free surface, and hence we expect some 'churn' at that surface as the motion of particles there are unconfined. Figure 20 shows the location of emerging large six-, seven-cycles. As in Fig. 19, this spatial distribution of six-, seven-cycle births shows the position of the centroid of each cycle at the time of its birth. It is useful to note here that the length scale of the emergent shear zone ($r = 8d_m$) is consistent with the length scale of information propagation to and from a sensor in a granular bed in [47]: just like this study, the sensor in [47] is of comparable size and has the same properties as the surrounding grains. Equally noteworthy is a recent study by Padbidri *et al.* [48] which showed that the propagation of grain rotation information through a granular assembly is strongly directionally dependent, and follows the alignment and distribution of force chains in the bed. They also uncovered a characteristic rotation transmission distance of approximately 5–10 grain diameters. This distance is consistent with both the grain sensor findings in [47], and the zone of influence found in the present work.

Based on the above findings, we can now offer a new perspective on dilatancy arising from the motion of a single

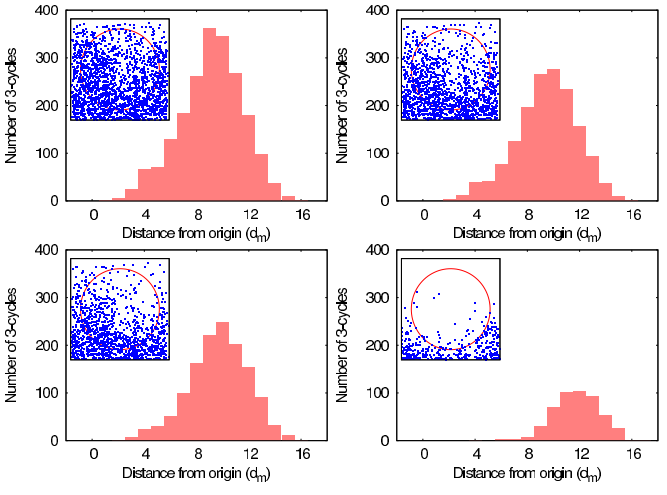

FIG. 18. (Color online) The population of persistent three-cycles in the bed drops steadily during the first stick phase (top left, top right, bottom left) before undergoing a sharp fall off following the first slip phase (bottom right). Images are separated by approximately 6 s (100 simulation timesteps). Note also the change in the spatial distribution of the three-cycle centroids after the slip. The insets show the spatial distribution of persistent three-cycles at each time, projected on to a plane at $y = 0$.

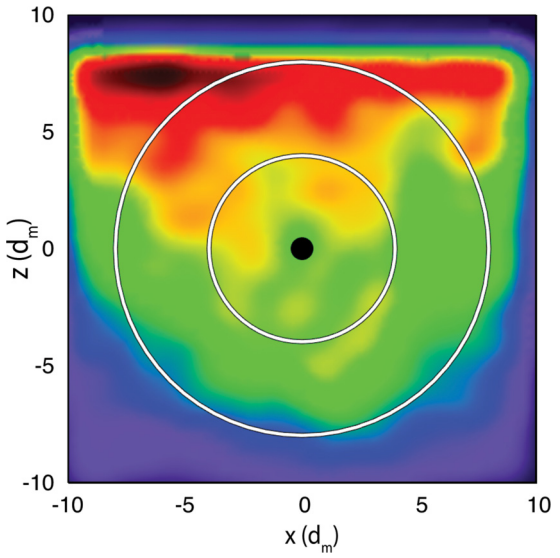

FIG. 19. (Color online) Spatial distributions of truss-like three-, four-, five-cycles undergoing contact cleavage during slip event. Truss-like three-, four-, five-cycles are represented by their centroid and at location determined from last time before cleavage. These centroids are projected on to a plane at $y = 0$. The large majority of contact cleavage occurs within $r = 8d_m$ of the intruder (the larger of the concentric circles) and along the top free surface of the bed.

grain intruder inside a granular bed. The phenomenon of dilatancy arises from the combined failure of three-, four-, five-cycles and force chain buckling. In the region ahead of the intruder, high porosity regions develop beside the intruder and towards the free surface of the bed; these regions are inhabited by large six-, seven-cycles formed from small three-, four-,

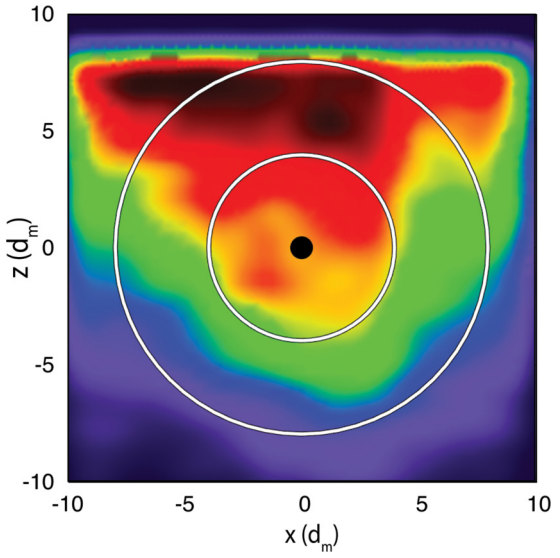

FIG. 20. (Color online) Spatial distributions of largest six-, seven-cycles in the bed, represented by their centroids. A projection of all six-, seven-cycle centroids on to a vertical plane ($y = 0$), plotted at their position when created. The large majority of six-, seven-cycles lie within $r = 8d_m$ of the intruder (the larger of the concentric circles), although dilation also occurs along the free top surface of the grain bed.

five-cycles cleaving and then joining together. The degradation of three-cycles in these regions destabilizes the force chains causing them to buckle. Buckling itself is an inherently dilatant process; furthermore, the energy released during buckling may induce additional dilatant rearrangements among weak neighbors.

3. Differences in force chains—fore and aft of the intruder

While we have made progress in understanding the shear and dilation zones of the granular bed driven by an intruder particle, we are still left with a puzzle: why is there a momentary peak in the average particle load vector magnitude of force chains *during* slip events? Recall from Fig. 10 that, while the average PLV drops over the entire slip event as expected, there are brief intervals during the slip when sharp bursts in average PLV occur. A potential explanation for this observation lies in another somewhat unusual behavior in the

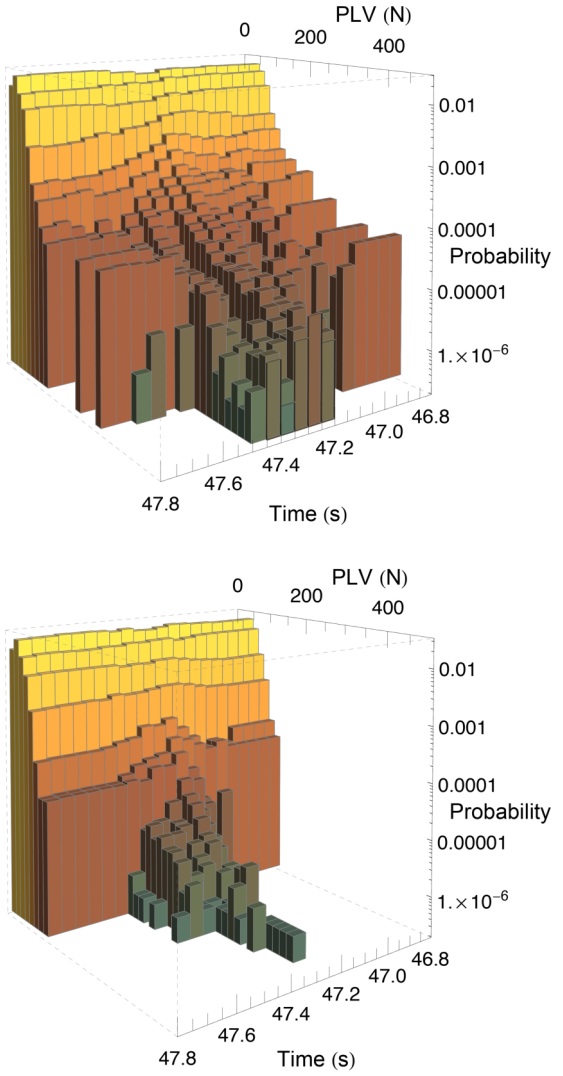

FIG. 21. (Color online) Calculating a probability distribution for the PLV of all the particles in the bed [split into fore (top) and aft (bottom)] during a slip event reveals the regions of increased load (both in space and time). The section of the bed aft of the intruder experiences a sharp peak in PLV around $t = 47.3$ s.

bed: the existence of buckling force chains behind the intruder with respect to the direction of the intruder's motion, as seen in Fig. 13. Our view of force chains—structures formed from the self-organization of the granular bed to resist the force being applied via the intruder—is insufficient to explain the development of these force chains behind the intruder, as the intruder does not apply force directly to this region. To understand this process, we turn to the distribution of PLVs in space and time, shown in Fig. 21. We split the bed in two equal halves: those particles that lie behind the intruder (with respect to its direction of motion), and those that lie ahead. We will refer to these regions as 'aft' and 'fore', respectively. Note the 'spike' in the average PLV in the aft (i.e., wake) region at around 47.3 s, during which multiple particles in the bed briefly experience very large PLVs that then quickly subside. This is a substantially different behavior from the next stick phase, during which the aft section of the bed essential returns to its original state. We therefore examine the force chains that form during the PLV spike, and that contain particles with a PLV in the range encompassed by the spike. This corresponds to a PLV above 150 N, which we will refer to as 'high-PLV'. We focus in on the first and largest spike in the PLV (from approximately 47.28 s to 47.35 s), which correspond to the first peak in Fig. 11 (top). For comparison the same analysis was applied to equal time intervals during the preceding and ensuing stick events. The results of this analysis can be seen in Fig. 22 for the region of the bed ahead of the intruder, and Fig. 23 for the wake region behind the intruder.

Figures 22 and 23 present the force chains containing high-PLV particles that are responsible for the peak in PLV during the slip. These high-PLV force chains are transient and mostly comprise short force chains of three particles. The behavior in the fore section of the bed are consistent with our previous results, arranged ahead of and below the intruder. They may be considered primary force chains, formed to oppose the motion of the intruder through the bed. However, the high-PLV chains in the aft section are aligned almost perpendicular to the

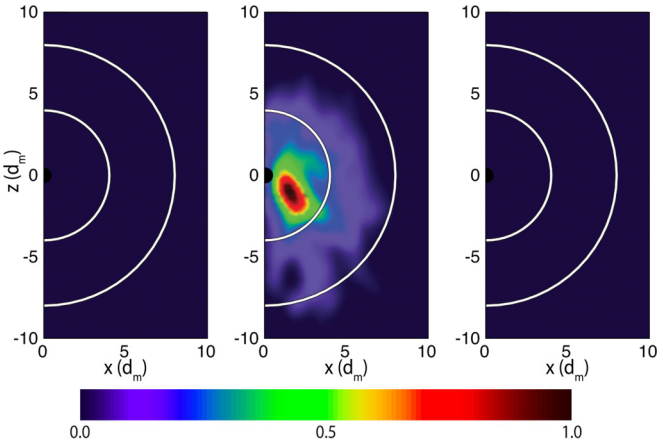

FIG. 22. (Color online) The fore region. Accumulated force chain births for high-PLV force chains in three different time periods, fore of the intruder. From left to right: prior to slip (end of first stick event), during slip, after slip (beginning of second stick event). The force chains are arranged as in previous results: ahead of and below the intruder, opposing its motion.

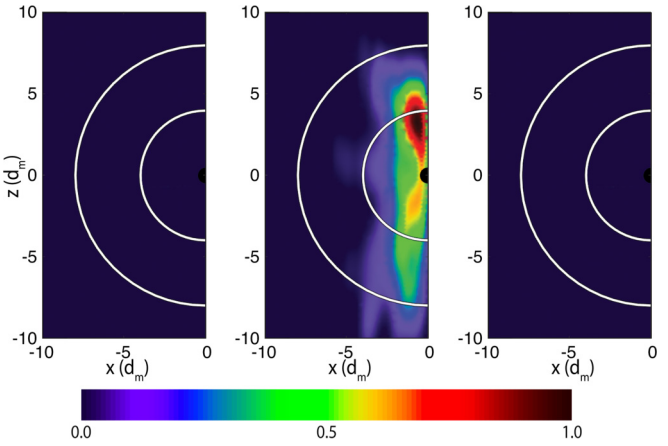

FIG. 23. (Color online) The wake region. Accumulated force chain births for high-PLV force chains in three different time periods, aft of the intruder. From left to right: towards the end of the first stick event prior to slip, during slip, after slip at the beginning of the second stick event). The force chains are aligned vertically and almost perpendicularly to the direction of motion of the intruder.

direction of the intruder's motion. These may be considered secondary force chains, formed by the effects of the intruder's passage rather than directly by the intruder itself. In this case, the alignment of the chains suggest they formed in response to vertical motion in the bed, for example, grains falling into the void left by the intruder, keeping in mind the intruder is of comparable size to the other grains. Finally, we found no evidence of any "dead-zone", i.e., an undeforming cluster of grains that move in rigid body motion with the intruder. This is perhaps not so surprising as the largest dimension of these zones tend to be less than that of the contact region between the intruder and the granular bed [43,44].

V. CONCLUSION

We characterized the mechanical response of a granular bed to an intruder grain that is of comparable size to the rest of the grains in the bed. This novel loading configuration leads to a response that bears both similarities and differences with those of other granular systems acted upon by solid bodies much larger than the grains in the bed. We found a well-defined shear zone, based on analysis of buckling force chains, and births and deaths of supporting n-cycles. Two such zones were identified: (i) an inner core that is within $r = 4d_m$ of the intruder position, where buckling force chains occurred; and (ii) an outer core extending to $r = 8d_m$ defined by the attrition of persistent three-cycles and dilation of the bed. We confirmed that the granular bed exhibits dilatant behavior, with small cycles cleaving throughout the $r = 8d_m$ zone, giving way to larger cycles in the same regions of the bed. The length scale of the emergent shear zone is consistent with the length scale of information propagation to and from "grain sensors", sensors of comparable size and properties as the grains themselves but was capable of recording and transmitting kinematic or force information [47]. We presented evidence for the formation of intermittent secondary force chains in the wake region of the bed, which manifest during

the slip events behind the intruder. These transient force chains are mostly short chains comprising three particles with high particle load vector magnitudes, arising as a side-effect of the passage of the intruder rather than as a direct response to the the intruder itself. Our analysis of stick-slip in a granular bed highlights the importance of examining granular systems at multiple spatial and temporal scales. Low temporal resolution data completely masked the rich behavior of the bed during the rapid slip events. Only by significantly increasing our time resolution were we able to uncover the novel behavior described herein. Future work will continue to focus on spatial and temporal effects, in particular, how the bed adapts its process of self-organization in response to changes in the intruder size, proximity to boundary walls, and free surface, as well as the prolonged repetitive passage of the intruder.

ACKNOWLEDGMENTS

We thank Jack Hopper for assistance in the preparation of this manuscript. We acknowledge the support of the Australian Research Council (Discovery Grant No. DP120104759), the US Army Research Office (Single Investigator Grant No. W911NF1110175), and the Melbourne Energy Institute.

[1] I. Albert, P. Tegzes, B. Kahng, R. Albert, J. G. Sample, M. Pfeifer, A. L. Barabási, T. Vicsek, and P. Schiffer, Phys. Rev. Lett. **84**, 5122 (2000).
[2] M. Knuth and C. Marone, Geochemistry Geophysics Geosystems **8**, Q03012 (2007).
[3] J. Geng and R. P. Behringer, Phys. Rev. E **71**, 011302 (2005).
[4] W. F. Brace and J. D. Byerlee, Science **153**, 990 (1966).
[5] J. D. Byerlee, Tectonophysics **9**, 475 (1970).
[6] S. Nasuno, A. Kudrolli, A. Bak, and J. P. Gollub, Phys. Rev. E **58**, 2161 (1998).
[7] I. Albert, P. Tegzes, R. Albert, J. G. Sample, A. L. Barabási, T. Vicsek, B. Kahng, and P. Schiffer, Phys. Rev. E **64**, 031307 (2001).
[8] C. M. Mate, G. M. McClelland, R. Erlandsson, and S. Chiang, Phys. Rev. Lett. **59**, 1942 (1987).
[9] E. G. Daub and J. M. Carlson, Phys. Rev. E **80**, 066113 (2009).
[10] K. E. Daniels and N. W. Hayman, J. Geophys. Res. **113**, B11411 (2008).
[11] D. Volfson, L. S. Tsimring, and I. S. Aranson, Phys. Rev. E **69**, 031302 (2004).
[12] J. R. Rice and S. T. Tse, J. Geophys. Res. **91**, 521 (1986).
[13] J. F. Métayer, D. J. Suntrup III, C. Radin, H. L. Swinney, and M. Schröter, Euruophys. Lett. **93**, 64003 (2011).
[14] N. W. Hayman, L. Ducloué, K. L. Foco, and K. E. Daniels, Pure Appl. Geophys. **168**, 2239 (2011).
[15] P. A. Johnson, H. Savage, M. Knuth, J. Gomberg, and C. Marone, Nature **451**, 57 (2008).
[16] K. Mair, K. M. Frye, and C. Marone, J. Geophys. Res. **107**, ECV 4-1 (2002).
[17] F. Radjai, D. E. Wolf, M. Jean, and J.-J. Moreau, Phys. Rev. Lett. **80**, 61 (1998).
[18] A. Tordesillas, Philos. Mag. **87**, 4987 (2007).
[19] A. Tordesillas, D. M. Walker, and Q. Lin, Phys. Rev. E **81**, 011302 (2010).
[20] D. W. Howell, R. P. Behringer, and C. T. Veje, Chaos: An Interdisciplinary J. Nonlinear Science **9**, 559 (1999).
[21] J. Zhang, T. S. Majmudar, A. Tordesillas, and R. P. Behringer, Granular Matter **12**, 159 (2010).
[22] A. Tordesillas, J. Zhang, and R. P. Behringer, Geomechanics and Geoengineering **4**, 3 (2009).
[23] R. Albert, M. A. Pfeifer, A. L. Barabási, and P. Schiffer, Phys. Rev. Lett. **82**, 205 (1999).
[24] J. E. Hilton and A. Tordesillas, Phys. Rev. E **88**, 062203 (2013).
[25] A. Tordesillas, D. M. Walker, G. Froyland, J. Zhang, and R. P. Behringer, Phys. Rev. E **86**, 011306 (2012).
[26] A. Tordesillas, Q. Lin, J. Zhang, R. P. Behringer, and J. Shi, J. Mech. Phys. Solids **59**, 265 (2011).
[27] D. M. Walker and A. Tordesillas, Int. J. Solids Struct. **47**, 624 (2010).
[28] L. Kondic, A. Goullet, C. S. O'Hern, M. Kramar, K. Mischaikow, and R. P. Behringer, Europhys. Lett. **97**, 54001 (2012).
[29] M. Kramar, A. Goullet, L. Kondic, and K. Mischaikow, Phys. Rev. E **87**, 042207 (2013).
[30] D. M. Walker, A. Tordesillas, M. Small, R. P. Behringer, and C. K. Tse, Chaos (to be published).
[31] J. E. Hilton, P. W. Cleary, and A. Tordesillas, AIP Conf. Proc. **1542**, 843 (2013).
[32] C. Thornton, S. J. Cummins, and P. W. Cleary, Powder Technol. **210**, 189 (2011).
[33] J. E. Hilton and P. W. Cleary, Phys. Rev. E **84**, 011307 (2011).
[34] G. W. Delaney, J. E. Hilton, and P. W. Cleary, Phys. Rev. E **83**, 051305 (2011).
[35] M. Muthuswamy and A. Tordesillas, J. Stat. Mech. Theor. Exp. (2006) P09003.
[36] J. F. Peters, M. Muthuswamy, J. Wibowo, and A. Tordesillas, Phys. Rev. E **72**, 041307 (2005).
[37] A. Tordesillas and M. Muthuswamy, J. Mech. Phys. Solids **57**, 706 (2009).
[38] B. Bollobás and O. Riordan, *Handbook of Large-Scale Random Networks* (Springer, Berlin, 2008), pp. 15–115.
[39] J. D. Horton, SIAM J. Comput. **16**, 358 (1987).
[40] K. Mehlhorn and D. Michail, ACM J. Experimental Algorithmics **11**, 1 (2006).
[41] A. Tordesillas, S. Pucilowski, L. Sibille, F. Nicot, and F. Darve, Philos. Mag. **92**, 4547 (2012).
[42] A. Tordesillas, S. Pucilowski, D. M. Walker, J. F. Peters, and M. Hopkins, Dynamics of Continuous, Discrete and Impulsive Systems-B **19**, 471 (2012).
[43] A. Tordesillas, C. A. H. Steer, and D. M. Walker, Nonlin. Processes Geophys. **21**, 505 (2014).
[44] T. G. Murthy, E. Gnanamanickam, and S. Chandrasekar, Phys. Rev. E **85**, 061306 (2012).
[45] J. Butlanska, M. Arroyo, A. Gens, and C. OSullivan, Canadian Geotechnical Journal **51**, 51 (2013).
[46] A. Tordesillas, S. Pucilowski, D. M. Walker, J. F. Peters, and L. Walizer, Int. J. Numer. Anal. Met. Geomechanics, doi:10.1002/nag.2258.
[47] D. M. Walker, A. Tordesillas, T. Nakamura, and T. Tanizawa, Phys. Rev. E **87**, 032203 (2013).
[48] J. M. Padbidri, C. M. Hansen, S. D. Mesarovic, and B. Muhunthan, J. Appl. Mech. **79**, 031011 (2012).